Journal of Engineering Mathematics **50:** 311–327, 2004.

Effect of inertia on the Marangoni instability of two-layer channel flow, Part I: numerical simulations

C. POZRIKIDIS
Department of Mechanical and Aerospace Engineering, University of California, San Diego, La Jolla, California 92093-0411, USA (cpozrikidis@ucsd.edu)

Received 2 December 2003; accepted in revised form 20 July 2004

Abstract. A numerical method is developed for simulating the flow of two superposed liquid layers in a two-dimensional channel confined between two parallel plane walls, in the presence of an insoluble surfactant. The algorithm combines Peskin's immersed-interface method with the diffuse-interface approximation, wherein the step discontinuity in the fluid properties is replaced by a transition zone defined in terms of a mollifying function. A finite-difference method is implemented for integrating the generalized Navier–Stokes equation incorporating the jump in the interfacial traction, and a finite-volume method is implemented for solving the surfactant transport equation over the evolving interface. The accuracy of the overall scheme is confirmed by successfully comparing the numerical results with the predictions of linear stability analysis and numerical simulations based on a boundary-element method for Stokes flow. Results for selected case studies suggest that inertial effects have a mild effect on the growth rate of the surfactant-induced Marangoni instability.

Key words: channel flow, immersed-interface method, liquid films, Marangoni instability, surfactants

1. Introduction

Linear stability analysis of two-layer channel flow with fluids of equal densities but different viscosities reveals that, in the absence of surfactants, the flow can be unstable provided that the Reynolds number is non-infinitesimal (*e.g.*, [1]). Two modes of instability have been identified: the first mode represents a shear-flow instability associated with the global structure of the shear flow, which arises at high Reynolds numbers irrespective of the relative fluid viscosities; the second mode describes Yih's [2] instability associated with the discontinuity in the shear rate due to the viscosity jump across the interface, which arises at arbitrarily small, but not precisely zero, Reynolds numbers.

Frenkel and Halpern [3,4] recently pointed out that an insoluble surfactant may have a further destabilizing influence by promoting the growth of interfacial waves in Stokes flow, even for fluids of equal viscosities. Conversely, a shear flow may destabilize an otherwise stable interface populated by surfactants. Blyth and Pozrikidis [5] reconsidered the linear stability problem in a broader framework that accounts for the effect of gravity and takes into consideration the surfactant diffusivity, and performed numerical simulations of the non-linear motion under the auspices of the lubrication approximation and in the context of Stokes flow. Their results confirmed the onset, and illustrated the non-linear stages of the instability.

Linear stability analysis for Stokes flow shows that the instability of the two-layer flow is determined by the properly non-dimensionalized shear rate of the unperturbed flow evaluated at the lower or upper side of the interface, denoted by s (see also [6]). In particular, the normal-mode analysis reveals the existence of two possible modes. When $s = 0$, both modes are stable, independent of the overall velocity profile; on the other hand, when s is non-zero,

one of the modes associated with Marangoni tractions due to surfactant nonuniformities may become unstable in a certain range of layer thickness and viscosity ratios, and for a certain range of wavenumbers. The prominence of the interfacial shear rate is consistent with physical intuition, suggesting that small enough deflections of the interface only feel the effect of the shear term in the local undisturbed velocity profile, as it appears in the surfactant transport equation.

The classical analysis of Yih, its subsequent extensions and refinements, and the recent findings of Frenkel, Halpern, Blyth and Pozrikidis reveal that three modes of instability are possible in the presence of an insoluble surfactant: the common high-Reynolds-number shear-flow instability, the finite-Reynolds-number Yih instability, and the Stokes-flow Marangoni instability. Under appropriate conditions, all three modes may arise, favoring the simultaneous growth of disturbances with different wavenumbers representing the respective most unstable modes.

Several authors have studied by numerical simulation the non-linear stages of the two-layer instability in a horizontal or inclined channel, in the absence of surfactants. Pozrikidis [7, 8] performed boundary-integral simulations of the two-layer Couette, Poiseuille, and gravity-driven flow at vanishing Reynolds number, and Coward *et al.* [9] and Li *et al.* [10] performed simulations based on the volume-of-fluid (VOF) method at low and moderate Reynolds numbers. The computations of Li *et al.* [10] confirmed the destabilizing influence of inertia, and revealed the occurrence of wave steepening and subsequent saturation due to finite-amplitude interactions. Similar simulations for selected case-studies were presented by Yiu and Chen [11], Zaleski *et al.* [12], Yecko and Zaleski [13], Tryggvason and Unverdi [14], and Zhang *et al.* [15] using the VOF, as well as the so-called "front tracking method", the latter being essentially Peskin's immersed-interface method discussed in Section 3 (*e.g.*, [16]).

In this article, the effect of fluid inertia on the Marangoni instability of the two-layer Couette flow is investigated by numerical simulation. The numerical method combines Peskin's immersed-interface formulation, the diffuse-interfaceapproximation, a variant of Chorin's projection method, and a finite-volume method for integrating the convection-diffusion equation governing surfactant transport. Two novel aspects of the algorithm are the computation of the mollifying function used to smear discontinuities in the physical properties of the fluids based on an integral identity, and the restatement of the effective force due to viscosity variations in terms of the viscosity gradient and the vorticity. The numerical results will suggest that the Marangoni instability persists at non-zero Reynolds numbers. In a companion article [6], a formal normal-mode linear stability analysis of the two-layer flow is undertaken, and the numerical methods developed in this article are applied to illustrate the non-linear evolution of exponentially growing perturbations consisting of two companion normal modes.

2. Problem statement

We consider the flow of two adjacent liquid layers in a horizontal channel confined between two parallel plane walls located at $y = \pm h$, as illustrated in Figure 1, and label the lower and upper fluid using, respectively, the indices 1 and 2. The lower and upper channel walls move parallel to themselves with velocities U_1 and U_2, generating a shear-driven flow that can be superposed on a pressure-driven flow induced by a specified streamwise pressure gradient. The interface is occupied by an insoluble surfactant with surface concentration Γ, which is convected and diffuses over the interface, but not into the bulk of the fluids, to alter the surface tension, γ. When the interface is flat and the surfactant concentration is uniform, we obtain

unidirectional flow with a piecewise linear-parabolic velocity profile. Our present interest lies in computing the evolution of the interface, and thereby assessing the stability of the two-layer flow, subject to periodic perturbations with wavelength L.

To describe the two-dimensional flow in the xy-plane, we introduce the generalized Navier–Stokes equation incorporating viscosity and density differences, as well as the jump in the traction across the interface due to the surface tension,

$$\rho\left(\frac{\partial \mathbf{u}}{\partial t}+\mathbf{u}\cdot\nabla\mathbf{u}\right)=-\nabla p+2\nabla\cdot(\mu\,\mathbf{E})-\int_I \mathcal{D}_2(\mathbf{x}-\mathbf{x}')\,\Delta\mathbf{f}(\mathbf{x}')\,\mathrm{d}l(\mathbf{x}'), \tag{2.1}$$

where $\mathbf{u}$ is the fluid velocity, p is the pressure, ρ is the density, μ is the viscosity, $\mathbf{E}\equiv(1/2)(\nabla\mathbf{u}+\nabla\mathbf{u}^T)$ is the rate-of-deformation tensor, $\mathcal{D}_2$ is Dirac's delta function in the xy-plane with dimensions of inverse squared length, and l is the arclength along the interface, which is denoted by I (*e.g.*, [17,18]). The expression inside the integral on the right-hand side of (2.1) involves the traction discontinuity across the interface, defined as

$$\Delta\mathbf{f}\equiv(\boldsymbol{\sigma}^{(1)}-\boldsymbol{\sigma}^{(2)})\cdot\mathbf{n}, \tag{2.2}$$

where $\boldsymbol{\sigma}$ is the Newtonian stress tensor, and $\mathbf{n}$ is the unit normal vector pointing into the lower fluid labeled 1, as illustrated in Figure 1. An interfacial force balance requires

$$\Delta\mathbf{f}=-\frac{\partial(\gamma\mathbf{t})}{\partial l}=\gamma\kappa\,\mathbf{n}-\frac{\partial\gamma}{\partial l}\,\mathbf{t}, \tag{2.3}$$

where γ is the position-dependent surface tension, $\mathbf{t}$ is the unit tangent vector pointing in the direction of increasing arclength l, and κ is the curvature of the interface in the xy-plane, reckoned to be positive when the interface is upward parabolic; with reference to Figure 1, $\kappa=-\mathbf{n}\cdot\mathrm{d}\mathbf{t}/\mathrm{d}l$.

The evolution of the surfactant concentration is governed by the convection–diffusion equation

$$\frac{\mathrm{d}\Gamma}{\mathrm{d}t}+\frac{\partial(u_t\,\Gamma)}{\partial l}-w\,\frac{\partial\Gamma}{\partial l}=-\Gamma\,\kappa\,u_n+D_s\frac{\partial^2\Gamma}{\partial l^2}, \tag{2.4}$$

where $u_t=\mathbf{u}\cdot\mathbf{t}$ and $u_n=\mathbf{u}\cdot\mathbf{n}$ are the interfacial velocities in the directions of the tangential and normal vectors, and D_s is the surface surfactant diffusivity (*e.g.*, [19,20]). The derivative $\mathrm{d}/\mathrm{d}t$ on the left-hand side of (2.4) expresses the rate of change of a variable following the

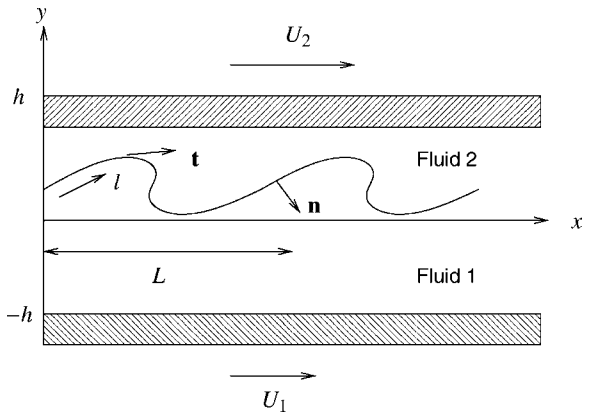

Figure 1. Schematic illustration of two-layer Couette–Poiseuille flow in a horizontal channel confined between two parallel plane walls moving parallel to themselves with velocities U_1 and U_2.

motion of interfacial nodes moving with the component of the fluid velocity normal to the interface and with an arbitrary tangential velocity $w(l)$. If $w=0$, the nodes reduce to marker points moving normal to the interface, whereas, if $w=u_t$, the nodes reduce to Lagrangian point particles moving with the local fluid velocity.

When the surfactant concentration is well below the saturation level, a linear relationship may be assumed between the surface tension and the surfactant concentration according to Gibbs' law, $\gamma_c-\gamma=\Gamma RT$, where R is the ideal gas constant, T is the absolute temperature, and γ_c is the surface tension of a clean interface which is devoid of surfactants (*e.g.*, [1,21]). Rearranging, we obtain the linear surface equation of state

$$\gamma=\gamma_c\left(1-\beta\,\frac{\Gamma}{\Gamma_0}\right), \tag{2.5}$$

where $\beta=\Gamma_0 RT/\gamma_c$ is a dimensionless coefficient related to the surface elasticity by $E=\gamma_c\beta/\Gamma_0$, and Γ_0 is a reference surfactant concentration corresponding to the surface tension $\gamma_0=\gamma_c(1-\beta)$. The importance of the surfactant on the interfacial dynamics is expressed by the dimensionless Marangoni number

$$\mathrm{Ma}\equiv\frac{E\Gamma_0}{\gamma_0}=\frac{\beta}{1-\beta}, \tag{2.6}$$

defined such that $\partial\gamma/\partial\Gamma=-\mathrm{Ma}\gamma_0/\Gamma_0$. This relation and the linear law (2.5) may also be used to describe small perturbations from the base concentration, Γ_0, with the understanding that the Marangoni number and associated coefficient β are no longer physiochemical constants, but express instead the surface elasticity as determined by the current conditions.

3. Numerical method

In the diffuse-interface approximation, the discontinuous density and viscosity fields are replaced by smoothed distributions defined in terms of a mollifying function $c(x,y)$, which takes the value of zero in the bulk of the lower layer, the value of unity in the bulk of the upper layer, and undergoes a gradual transition across the interface. The mollified viscosity field is described as

$$\mu(\mathbf{x})=\mu_1+(\mu_2-\mu_1)\,c(\mathbf{x}), \tag{3.1}$$

and the density is given by a corresponding expression.

In previous implementations of the immersed interface method, the mollifying function was computed on the basis of the following exact integral representation for the gradient,

$$\nabla c(\mathbf{x})=-\int_I \mathcal{D}_2(\mathbf{x}-\mathbf{x}')\,\mathbf{n}(\mathbf{x}')\,\mathrm{d}l(\mathbf{x}'). \tag{3.2}$$

Smoothing the delta function as will be discussed in Section 3.3, and taking the divergence of the resulting equation, we derive a Poisson equation for c. The forcing term is the divergence of a nearly-singular vector field distributed along the interface (*e.g.*, [17]). The solution can be found using a finite-difference method on the same grid used for solving the equation of motion.

In the present implementation, the mollifying function is computed by a new method that is independent of the domain discretization adopted for solving the hydrodynamics, based on the integral representation

$$c(\mathbf{x})=1-\frac{1}{c_1}\Big(\int_{I_p}\mathbf{n}(\mathbf{x}')\cdot\nabla' G_\delta(\mathbf{x}',\mathbf{x})\,\mathrm{d}l(\mathbf{x}')+c_2\Big), \tag{3.3}$$

where I_p is one period of the interface, and ∇' is the gradient operating with respect to $\mathbf{x}'$. The parameters c_1 and c_2 are adjusted to ensure that $c(x, y)$ reaches a minimum of 0 and a maximum of 1, respectively, on the lower or upper wall. The kernel $G_\delta(\mathbf{x}', \mathbf{x})$ is a modification of the periodic Neumann function of Laplace's equation in two dimensions whose normal derivative vanishes over the upper wall located at $y = h$, given by

$$G_\delta(\mathbf{x}', \mathbf{x}) = -\frac{1}{4\pi} \log \frac{\cosh[k(y'-y)] - \cos[k(x'-x)] + \delta^2}{\cosh[k(y'-2h+y)] - \cos[k(x'-x)] + \delta^2}, \tag{3.4}$$

where $k = 2\pi/L$ is the wavenumber, and δ is a numerical dimensionless parameter determining the spreading thickness of the interfacial layer, scaled with respect to the wavelength L. When $\delta = 0$, the mollifying function $c(x, y)$ undergoes a step discontinuity across the interface.

In the numerical method, the line integral over the interface on the right-hand side of (3.3) is evaluated using the trapezoidal rule with eight divisions over individual interfacial cubic-spline segments, as will be discussed in Section 3.1. The gradient of the mollifying function is computed numerically by central difference approximations. In the numerical simulations based on a finite-difference scheme discussed later in this section, the spreading parameter is set to $\delta = 0{\cdot}5\, k\, \Delta x$, where Δx is the spacing of a finite-difference grid in the streamwise direction. Figure 2(a) shows a typical graph of the mollifying function over one period of the flow, for $L = 2h$, and smearing parameter $\delta = 0{\cdot}5\, k\, \Delta x$. In this figure, the separation between two adjacent grid lines is $\Delta x = \Delta y = L/64 = h/32$; as expected, the transition layer across the interface occupies approximately four cells.

The method for computing the mollifying function described in this section can be readily generalized to other two- and three-dimensional flow configurations by a straightforward substitution for the Green's function. Consider, for example,two-dimensional flow in a channel containing a periodic array of drops or bubbles separated by the distance L (*e.g.*, [17]). In this case, the mollifying function can be computed from the integral representation

$$c(x, y) = -\frac{1}{c_1}\Big(\int_C \mathbf{n}(\mathbf{x}') \cdot \nabla G_\delta(\mathbf{x}' - \mathbf{x})\, \mathrm{d}l(\mathbf{x}') + c_2 \Big), \tag{3.5}$$

where C is the interface of one drop, $\mathbf{n}$ is the unit vector normal to the interface pointing into the suspending fluid,

$$G_\delta(\mathbf{x}' - \mathbf{x}) = -\frac{1}{4\pi} \log \Big[\cosh[k(y'-y)] - \cos[k(x'-x)] + \delta^2 \Big] \tag{3.6}$$

is the desingularized, singly periodic Green's function of Laplace's equation in the xy-plane, and $k = 2\pi/L$ is the wavenumber. The parameters c_1 and c_2 are adjusted to ensure that $c(x, y)$ reaches a minimum value of 0 far from drop interfaces, and a maximum value of 1 near the center of each drop. Figure 2(b) shows a typical graph of the mollifying function over two periods for smearing parameter $\delta = 0{\cdot}5\, k\, \Delta x$.

3.1. Interface representation

In the numerical implementation, one period of the interface is described by N_I interfacial nodes, denoted as $\mathbf{x}_k$, $k = 1, \ldots, N_I$, shown as circles in Figure 3. The shape of the interface is then reconstructed using cubic-spline interpolation with periodic boundary conditions for the first and second derivatives, and is described as $x(l_p), y(l_p)$. At the nodes, the interpolation variable l_p is identified with the current length of the polygonal line connecting adjacent nodes and measured from the first node. The solution of the nearly tridiagonal system

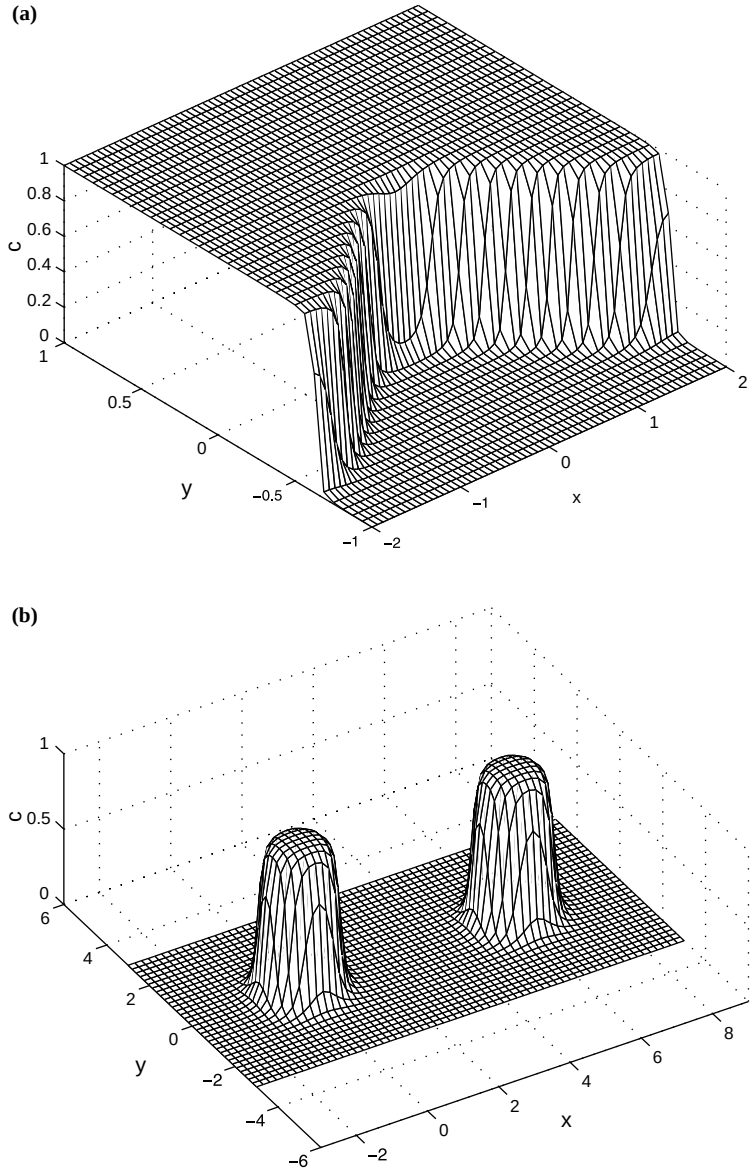

Figure 2. Graph of the mollifying function for (a) a two-layer channel flow with a sinusoidal interface of wavelength $L=4h$, (b) flow in a channel containing a periodic array of drops. In both cases, the smearing parameter is set to $\delta=0{\cdot}5k\,\Delta x$, where Δx is the horizontal grid spacing.

of algebraic equations for the cubic-spline coefficients is found efficiently using a modification of Thomas's algorithm (*e.g.*, [22]). After the interpolation has been concluded, the normal and tangential vectors are computed using standard formulae of differential geometry, and the curvature of the interface in the xy-plane is calculated using the formula

$$\kappa=-\frac{x''y'-y''x'}{(x'^2+y'^2)^{3/2}}, \tag{3.7}$$

where a prime denotes a derivative with respect to l_p.

To ensure adequate spatial resolution and an even point distribution along the interface at all times, the interfacial nodes are redistributed after each time step so that the arc length

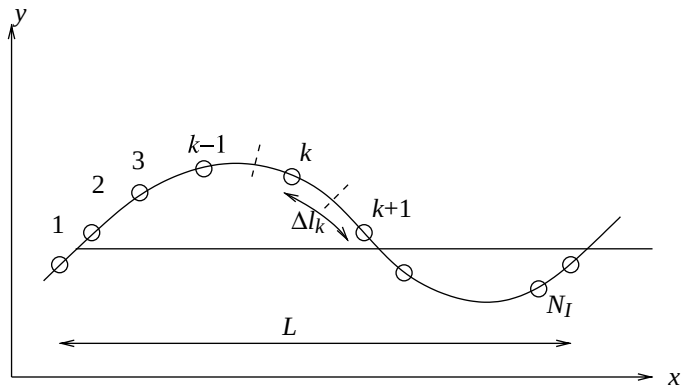

Figure 3. The interface is reconstructed by cubic-spline interpolation based on adaptively distributed interfacial nodes, shown as circles.

between the adjacent nodes k and $k+1$, denoted as $\Delta l_k \equiv l_{k+1} - l_k$, lies within two specified bounds, $\Delta_{\min} < \Delta l_k < \Delta_{\max}$. In the numerical computations presented in this article, $\Delta_{\min}$ was set to a value in the range $0{\cdot}5\Delta x$ – $1{\cdot}5\Delta x$, while $\Delta_{\max}$ was set to $2{\cdot}0\Delta x$. These choices ensure that (a) the interfacial nodes are not crowded inside a grid cell, (b) the projection of the last term on the left-hand side of (2.1) onto the grid yields a smoothly varying field, as will be discussed in Section 3.2, and (c) refining the grid size enforces a higher spatial resolution for the interface. In addition, the aperture angle associated with each node, $\Delta\theta_k \equiv \kappa_k(\Delta l_{k-1} + \Delta l_k)$, is required to be less than a specified threshold, where κ_k is the curvature of the interface at the kth node. If the node separation Δl_k is too small, nodes k and $k+1$ are removed and replaced by a midway node, provided that the new point distribution is consistent with the aforementioned criteria on the maximum point separation and aperture angle. When new interfacial nodes are introduced, their position and the local surfactant concentration are computed by cubic-spline interpolation.

3.2. Finite-difference method

Having smoothed the physical properties of the fluids across an artificial interfacial transition zone, we use the continuity equation to recast the generalized equation of motion (2.1) into the form

$$\rho \frac{\partial \mathbf{u}}{\partial t} + \rho \left(\mathbf{u} - \frac{2}{\rho}\nabla\mu\right) \cdot \nabla\mathbf{u} = -\nabla p + \mu \nabla^2 \mathbf{u} + \nabla\mu \times \boldsymbol{\omega} - \int_I \mathcal{D}_2(\mathbf{x} - \mathbf{x}')\, \Delta\mathbf{f}(\mathbf{x}')\, \mathrm{d}l(\mathbf{x}'), \tag{3.8}$$

where $\boldsymbol{\omega} \equiv \nabla \times \mathbf{u}$ is the vorticity. It is worth noting that the third term on the right-hand side of (3.8) contributes a term that is tangential to the interface.

In the immersed-interface method (IIM) inspired by Peskin's immersed-boundary method (IBM) [24] and coined "front tracking" by subsequent authors, the integral on the right-hand side of the generalized equation of motion (3.8) is approximated by the trapezoidal rule, setting

$$\int_I \mathcal{D}_2(\mathbf{x} - \mathbf{x}')\, \Delta\mathbf{f}\, \mathrm{d}l(\mathbf{x}') \simeq \sum_{k=1}^{N_I} \mathcal{D}_2(\mathbf{x} - \mathbf{x}_k)\, \mathbf{F}_k, \tag{3.9}$$

where

$$\mathbf{F}_k \equiv \int_{E_k} \Delta\mathbf{f}\, \mathrm{d}l(\mathbf{x}'), \tag{3.10}$$

and E_k is an interfacial element associated with the kth node, enclosed by the dashed lines in Figure 3. Summation is implied over the infinite repetition of periodic images of the interfacial elements on the right-hand side of (3.9).

To compute the nodal force $\mathbf{F}_k$, we may apply the trapezoidal rule, obtaining

$$\mathbf{F}_k = \Delta\mathbf{f}_k \, \frac{l_{k+1} - l_{k-1}}{2}, \tag{3.11}$$

where $\Delta\mathbf{f}_k$ is the jump in the interfacial traction evaluated at the kth node. The Marangoni traction expressed by the second term on the right-hand side of (2.3) can be evaluated from the cubic-spline interpolation with respect to the polygonal arc length l_p as $\partial\gamma/\partial l = (\partial\gamma/\partial l_p)\,(\partial l_p/\partial l)$. An alternative method based on the middle expression in (2.3) is implemented by the approximation

$$\mathbf{F}_k = -\Big(\frac{\mathbf{x}_{k+1} - \mathbf{x}_k}{|\mathbf{x}_{k+1} - \mathbf{x}_k|} \, \frac{\gamma_{k+1} + \gamma_k}{2} - \frac{\mathbf{x}_k - \mathbf{x}_{k-1}}{|\mathbf{x}_k - \mathbf{x}_{k-1}|} \, \frac{\gamma_k + \gamma_{k-1}}{2} \Big). \tag{3.12}$$

This method has the important feature that the discrete force balance

$$\sum_{k=1}^{N_I} \mathbf{F}_k = \mathbf{0}, \tag{3.13}$$

is satisfied to machine precision. In practice, we find that while the first method based on (3.11) works well for a clean interface, the second method based on (3.12) is preferable in the presence of surfactants.

Next, the delta function associated with the kth node is replaced with a smooth function that is supported by a rectangular region centered at the kth node. This is done by introducing the approximation

$$\mathcal{D}_2(\mathbf{x}) \simeq \mathcal{H}(\mathbf{x}) \equiv \frac{1}{16\Delta x\, \Delta y} (1 + \cos\hat{x})(1 + \cos\hat{y}), \tag{3.14}$$

for $x_k - 2\Delta x < x < x_k + 2\Delta x$ and $y_k - 2\Delta y < y < y_k + 2\Delta y$, where $\hat{x} \equiv \pi x/(2\Delta x)$, $\hat{y} \equiv \pi y/(2\Delta y)$, and Δx, Δy are the spatial discretization intervals in the streamwise and lateral directions. Note that the integral of $\mathcal{H}(\mathbf{x})$ over the entire xy-plane is equal to unity, as required. Substituting (3.14) in (3.9) and the result in (3.8), we obtain

$$\rho \, \frac{\partial \mathbf{u}}{\partial t} + \rho \left(\mathbf{u} - \frac{2}{\rho} \nabla\mu \right) \cdot \nabla\mathbf{u} = -\nabla p + \mu \nabla^2 \mathbf{u} + \nabla\mu \times \boldsymbol{\omega} + \mathcal{B}(\mathbf{x}), \tag{3.15}$$

where

$$\mathcal{B}(\mathbf{x}) \equiv -\sum_{k=1}^{N_I} \mathcal{H}(\mathbf{x} - \mathbf{x}_k)\, \mathbf{F}_k. \tag{3.16}$$

As previously, summation is implied over the infinite repetition of periodic images of the interfacial nodes.

Having smoothed out the physical properties of the fluid and the singular term on the right-hand side of (3.8), we compute the evolution of the flow subject to an initial condition

using a variation of Chorin's projection method. The algorithm involves a number of elementary sub-steps based on the constituent evolution equations

$$\begin{aligned}
&\rho \frac{\partial \mathbf{u}}{\partial t} = -\frac{\Delta p}{L}\,\mathbf{e}_x + \nabla\mu \times \boldsymbol{\omega} + \mathcal{B}(\mathbf{x}),\\
&\rho\left(\frac{\partial \mathbf{u}}{\partial t} + \mathbf{v}\cdot\nabla\mathbf{u}\right) = \mu\,\nabla^2\mathbf{u},\\
&\rho \frac{\partial \mathbf{u}}{\partial t} = -\nabla\phi,
\end{aligned} \tag{3.17}$$

where $\mathbf{v} \equiv \mathbf{u} - (2/\rho)\,\nabla\mu$, Δp is a specified pressure drop across each period of length L, $\mathbf{e}_x$ is the unit vector along the x axis, and ϕ is a projection function, regarded as an approximation to the non-periodic part of the pressure (*e.g.*, [18,23]). To expedite the simulations, the second step is further decomposed into the one-dimensionalconvection–diffusion steps,

$$\rho\left(\frac{\partial \mathbf{u}}{\partial t} + v_x\,\frac{\partial \mathbf{u}}{\partial x}\right) = \mu\,\frac{\partial^2 \mathbf{u}}{\partial x^2}, \qquad \rho\left(\frac{\partial \mathbf{u}}{\partial t} + v_y\,\frac{\partial \mathbf{u}}{\partial y}\right) = \mu\,\frac{\partial^2 \mathbf{u}}{\partial y^2}. \tag{3.18}$$

The first sub-step is executed subject to the streamwise periodicity condition, whereas the second sub-step is executed subject to the no-penetration and a properly designed slip-boundary condition, as will be discussed later in this section (*e.g.*, [18,23]).

The governing equations were integrated in time using a finite-difference method on a uniform grid. Specifically, the first equation in (3.17) was integrated using the explicit Euler method, and Equations (3.18) were integrated using the implicit Crank–Nicolson method. The latter requires solving tridiagonal systems of linear equations for carrying out the y integration, and nearly-tridiagonal systems of linear equations with two bordering elements due to the periodicity condition for carrying out the x integration. The solution of these systems can be found efficiently using the standard or a modified version of the Thomas algorithm (*e.g.*, [22]).

Demanding that the third equation in (3.17) delivers a solenoidal velocity field at the end of a complete time step, we derive a generalized Poisson equation for the projection function,

$$\nabla\cdot\left(\frac{1}{\rho}\,\nabla\phi\right) = \frac{1}{\Delta t}\,\nabla\cdot\mathbf{u}^*, \tag{3.19}$$

where $\mathbf{u}^*$ is the velocity at the end of the convection-diffusion step. The solution is found subject to the streamwise periodicity condition and the homogeneous Neumann boundary condition at the lower and upper wall. In the computations discussed in this article, the densities of the lower and upper fluid are identical, and the projection satisfies the Poisson equation

$$\nabla^2\phi = \frac{\rho}{\Delta t}\,\nabla\cdot\mathbf{u}^*. \tag{3.20}$$

In the numerical implementation, the linear system arising from the central-differencing discretization of (3.20) was solved by standard Gauss–Seidel iteration.

To ensure the exact satisfaction of the no-slip boundary condition at the upper and lower wall at the end of the projection step, advancement over each time step is carried out in an iterative fashion, where the wall boundary condition for the intermediate velocity at the y convection–diffusion step is gradually modified in anticipation of the $O(\Delta t)$ slip velocity introduced in the projection step (*e.g.*, [18,23]). In practice, because the slip velocity is transferred from the previous step, only one or two iterations are necessary to reduce the numerical slip velocity down to the level of the round-off error.

3.3. Marker point motion

Once the velocity field has been updated over a time step, the interfacial marker points are advanced in time under the action of an interpolated velocity field using Euler's explicit method. In the numerical simulations discussed later in this article, the interfacial nodes and their interpolated offsprings are Lagrangian point particles convected with the fluid velocity.

A widely used method of computing the node velocity is based on Peskin's [24,16] interpolation formula

$$\mathbf{u}(\mathbf{x}) = \sum_{i,j} \mathcal{H}(\mathbf{x} - \mathbf{x}_{ij})\, \mathbf{u}_{i,j}\, \Delta x\, \Delta y, \tag{3.21}$$

where $\mathbf{u}_{ij}$ is the velocity at the (i, j) grid point [24]. One weakness of this scheme is the inability to produce a spatially uniform field from uniform grid values.

To circumvent this difficulty, we carry out the interpolation using the bicubic B-spline approximation in the x and y directions, based on the formula

$$\mathbf{u}(\mathbf{x}) = \sum_{l_x=-1}^{2} \sum_{l_y=-1}^{2} \mathbf{u}_{i+l_x, j+l_y}\, w_{l_x}(\xi_x)\, w_{l_y}(\xi_y), \tag{3.22}$$

where the point $\mathbf{x}$ lies inside the cell confined between the i and $i+1$ vertical, and the j and $j+1$ horizontal grid lines. The arguments of the interpolation functions are $\xi_x \equiv (x - x_{i,j})/\Delta x$, and $\xi_y \equiv (y - y_{i,j})/\Delta y$. The uniform B-spline interpolation functions are given by (*e.g.*, [22])

$$\begin{aligned} w_{-1}(\xi) &= \tfrac{1}{6}(1-\xi)^3, \qquad w_0(\xi) = \tfrac{1}{6}(4 - 6\xi^2 + 3\xi^3), \\ w_1(\xi) &= \tfrac{1}{6}(1 + 3\xi + 3\xi^2 - 3\xi^3), \qquad w_2(\xi) = \tfrac{1}{6}\xi^3. \end{aligned} \tag{3.23}$$

A distinguishing property of these functions is that their sum is equal to unity for any argument value, ξ.

3.4. Surfactant transport

The convection–diffusion equation for the surfactant (2.4) is treated simultaneously using a finite-volume method (*e.g.*, [20,5]). In particular, following or preceding the advancement of the interfacial nodes, the ordinary differential equations originating from the finite-volume discretization are integrated in time using a semi-implicit method, where the interfacial velocity and geometrical properties of the interface are evaluated at the beginning of each time step.

4. Leveling of an interface

The performance and accuracy of the numerical method described in Section 3 was assessed by comparing the results of numerical simulations with the predictions of linear stability theory, as well as with the results of simulations based on a boundary-element method for Stokes flow presented by Blyth and Pozrikidis [5]. By way of carrying out this investigation, we consider the leveling of the interface separating two fluids with equal densities under the action of surface tension in an otherwise quiescent environment, that is, for vanishing overall streamwise pressure gradient and wall velocities. The undisturbed lower and upper layer thicknesses are $h_1 = h + y_0$ and $h_2 = h - y_0$, where y_0 is the position of the flat interface. The perturbation is introduced by displacing the interface to a position described by

$$y(x, t=0) = y_0 + \epsilon\, h \cos kx, \tag{4.1}$$

where $k = 2\pi/L$ is the wave number, and ϵ is the dimensionless amplitude of the disturbance. The initial velocity is taken to be zero within both fluids. Physically, capillary forces imparted to the fluid by the corrugated interface act as a narrow band of a distributed body force that tends to restore the flat shape.

First, we consider the motion in the absence of surfactants, setting $\beta = 0$. Figure 4 shows the evolution of the interface amplitude, a, plotted against the dimensionless time $\tau \equiv t\gamma/(\mu h)$ on a log-linear scale, for viscosity ratios $\lambda \equiv \mu_2/\mu_1 = 1$ and 0·2. In this graph, the instantaneous amplitude has been normalized by the initial amplitude, $a_0 \equiv \epsilon h$. The unperturbed interface is located at $y_0 = -h/3$, yielding a layer thickness ratio $r \equiv h_2/h_1 = 2$, the wave length of the interfacial wave is $L/h = 4$, and the initial amplitude of the interface is $\epsilon = 0{\cdot}20$. Unless

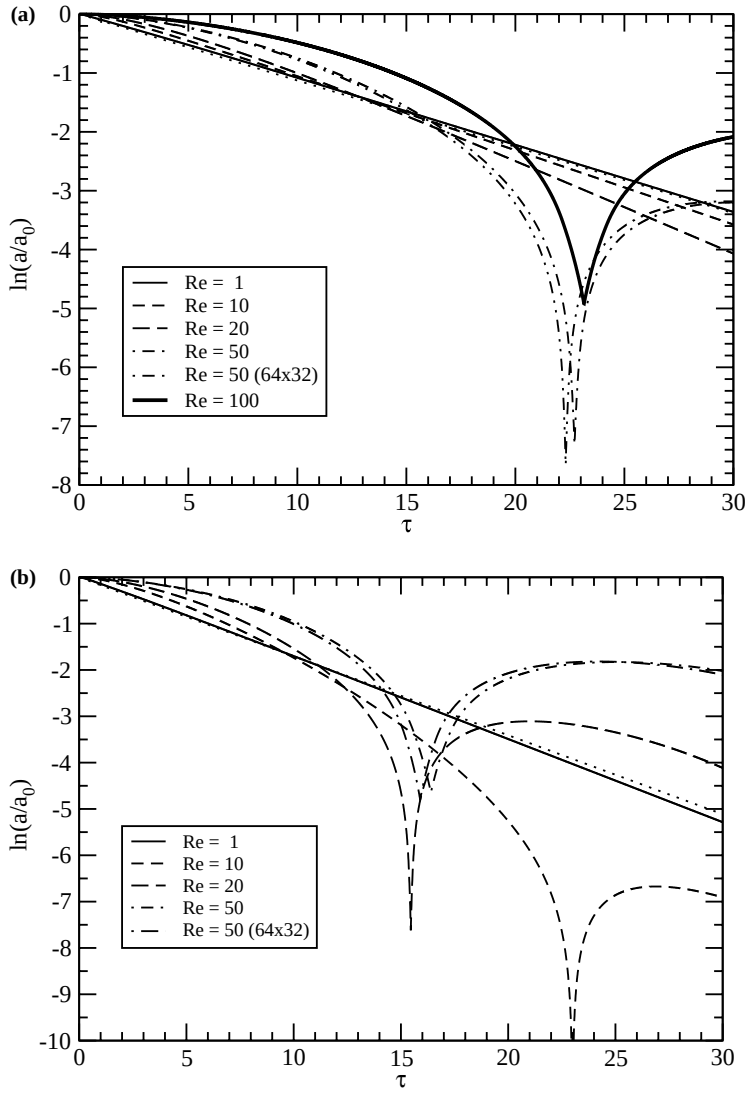

Figure 4. Leveling of the interface under the action of surface tension in an otherwise quiescent environment, in the absence of surfactants, for $h_2/h_1 = 2$, $L/h = 4$ and viscosity ratio (a) $\mu_2/\mu_1 = 1$ and (b) 0·2. The straight dotted lines represent the predictions of linear stability theory for Stokes flow.

noted otherwise, all simulations were conducted on a standard 32×16 grid with dimensionless time step $\Delta\tau = 0{\cdot}005$. Results are presented for several Reynolds numbers, $\mathrm{Re} \equiv \rho_1 \gamma h/\mu_1^2$, and two grid sizes. The duplicate results for $\mathrm{Re} = 50$ shown in the figure demonstrate that increasing the grid size from 32×16 to 64×32 has only a mild effect on the accuracy of the simulations. The comparison confirms that the salient figures of the motion are well reproduced by the low-resolution simulation.

The straight dotted line with slope $-0{\cdot}112744$ in Figure 4(a) represents thepredictions of linear stability analysis for Stokes flow, revealing the existence of a single exponentially decaying normal mode (*e.g.*, [5]). The numerical results for $\mathrm{Re} = 1$ are in excellent agreement with this theoretical estimate, even though the amplitude of the perturbation is not infinitesimal. As the Reynolds number is raised, the rate of decay of the perturbation is initially reduced. Physically, the fluid must pick up enough momentum to overcome its inertia. At long times, the interface exhibits damped oscillations with an angular frequency that depends on the Reynolds number. In the theoretical limit of infinite Reynolds number, the interface will exhibit undamped oscillations in the form of a standing capillary wave. Similar behavior is observed for viscosity ratio $\lambda = 0{\cdot}2$, as illustrated in Figure 4(b). The straight dotted line with slope $-0{\cdot}170458$ in this figure represents the predictions of linear stability analysis for Stokes flow, which is in excellent agreement with the results of the simulations for $\mathrm{Re} = 1$. At higher Reynolds numbers, damped oscillations arise.

Next, we consider flow in the presence of a surfactant, and specify that the initial surfactant concentration has a sinusoidal distribution described by

$$\Gamma(x, t = 0) = \Gamma_0 \Big[1 + \epsilon_\Gamma \cos(kx - \phi_\Gamma) \Big], \tag{4.2}$$

where Γ_0 is the unperturbed surfactant concentration, ϵ_Γ is the dimensionless amplitude of the perturbation, and ϕ_Γ is the phase-shift of the surfactant concentration wave with respect to the initial interfacial displacement described by (4.1). Figure 5 shows results of simulations for layer thickness ratio $r = 2$, unit viscosity ratio, $\lambda = 1$, surfactant sensitivity parameter, $\beta = 0{\cdot}5$, corresponding to Marangoni number $\mathrm{Ma} = 1$, vanishing surfactant diffusivity, $D_s = 0$, and $\epsilon = 0{\cdot}2$, $\epsilon_\Gamma = 0{\cdot}1$, $\phi_\Gamma = 0{\cdot}0$. The dotted line in Figure 5(a) represents the prediction of linear theory for Stokes flow in the absence of surfactants, while the dashed line labeled BEM represents the results of a numerical simulation for Stokes flow conducted by Blyth and Pozrikidis's boundary-element method [5]. The results of the finite-difference code for $\mathrm{Re} = 1$ are in good agreement with those of the boundary-element simulation. Comparing Figure 5 with Figure 4, we find that the surfactant has a significant influence on the dynamics of the motion, especially at the higher Reynolds numbers considered where oscillations arise. Figure 5(b, c) shows instantaneous velocity vector fields for $\mathrm{Re} = 1$ and 50, respectively, at dimensionless times $\tau = 10{\cdot}085$ and $10{\cdot}005$, revealing subtle differences concerning, for example, the location of the center of the viscous eddies mediating the leveling action.

Overall, the results presented in Figures 4 and 5 provide assurance for the reliability of the immersed-interface method implemented in the finite-difference code, in the absence as well as in the presence of surfactants.

5. Stability of the two-layer channel flow

Having developed and tested the numerical methods, we turn our attention to the instability of the unidirectional, two-layer flow. The unperturbed velocity profiles in the upper and lower layer are given, respectively, by

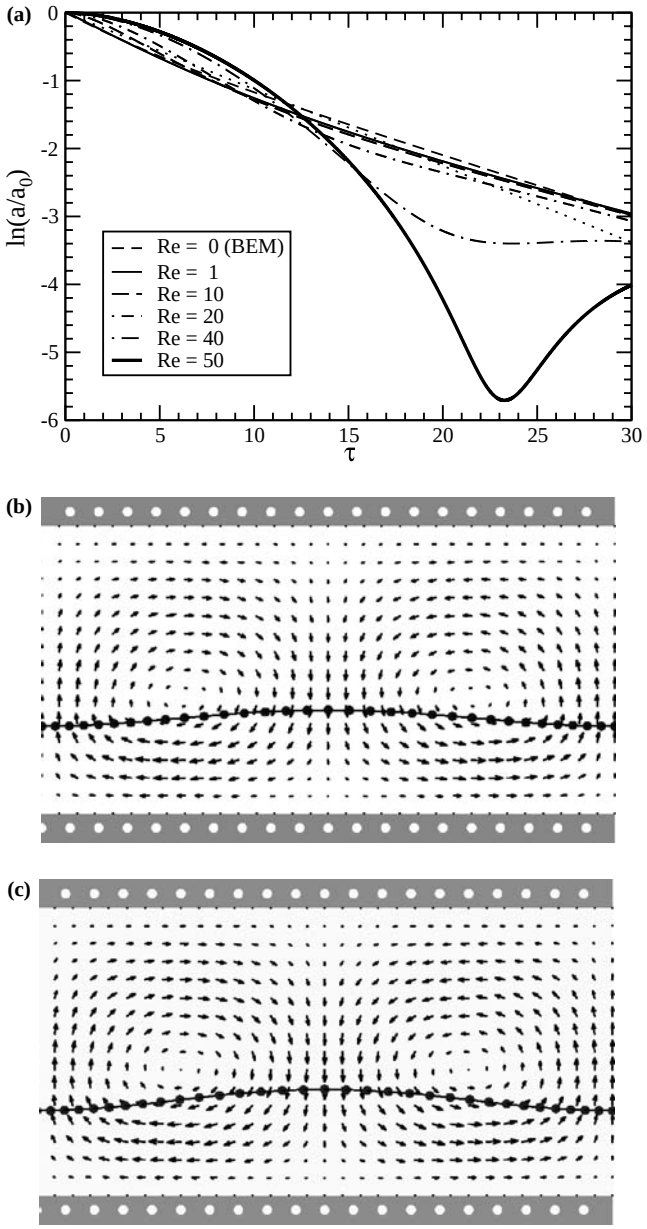

Figure 5. Leveling of the interface between two layers in a horizontal channel under the action of surface tension: (a) decay of the interfacial wave in the presence of surfactants; (b, c) instantaneous interfacial shape and velocity vector field for (b) Re = 1 at time $\tau = 10{\cdot}085$, and (c) Re = 50 at time $\tau = 10{\cdot}005$.

$$u_x = -\frac{\chi}{2\mu_1}(y-y_0)^2 + \xi_1 (y-y_0) + u_I, \quad \text{for } -h < y < y_0,$$
$$u_x = -\frac{\chi}{2\mu_2}(y-y_0)^2 + \xi_2 (y-y_0) + u_I, \quad \text{for } y_0 < y < h, \tag{5.1}$$

where $\chi \equiv -\partial p/\partial x$ is the negative of the streamwise pressure gradient, y_0 is the position of the undisturbed interface, u_I is the interfacial velocity given by

$$u_I = \frac{h_1 h_2}{2\mu_1}\frac{1+r}{\lambda+r}\chi + \frac{r U_1 + \lambda U_2}{r+\lambda}, \tag{5.2}$$

$\lambda \equiv \mu_2/\mu_1$ is the viscosity ratio, $r \equiv h_2/h_1$ is the ratio of the unperturbed layer thicknesses, and

$$\xi_1 = -\frac{\chi h_1}{2\mu_1} + \frac{u_I - U_1}{h_1}, \qquad \xi_2 = \frac{\xi_1}{\lambda} = \frac{\chi h_2}{2\mu_2} - \frac{u_I - U_2}{h_2} \tag{5.3}$$

are the interfacial shear rates in the lower and upper fluid.

In one series of simulations, the unperturbed unidirectional flow described by (5.1) was adopted as an initial condition. To initiate the perturbation, the interface was maintained horizontal by setting $\epsilon = 0$ in (4.1), while a periodic perturbation in the surfactant concentration was introduced according to (4.2). The associated Marangoni tractions cause the interface to deform into a sinusoidal wave whose amplitude initially grows, and eventually may grow or decay depending on the flow conditions determining the stability of the base flow.

Figure 6 illustrates the effect of the Reynolds number, $\mathrm{Re} = \rho_1 |U_2 - U_1| h/(2\mu_1)$, on the growth of an interfacial wave with wavelength $L/h = 6$ in Couette flow, $\chi = 0$, for layer thickness ratio $r = 2$, viscosity ratio $\lambda = 0{\cdot}5$, and negligible surfactant diffusivity, $D_s = 0$. The initial amplitude of the surfactant concentration wave is $\epsilon_\Gamma = 0{\cdot}5$, the surfactant sensitivity parameter is set to $\beta = 0{\cdot}5$, and the capillary number is $\mathrm{Ca} \equiv \mu_1 \Delta U/\gamma_0 = 2$, where $\Delta U = U_2 - U_1$, and γ_0 is the surface tension of the undisturbed interface corresponding to the unperturbed surfactant concentration Γ_0. In these simulations, the dimensionless time step is set to $\Delta\tau = 0{\cdot}005$, where the dimensionless time is defined as $\tau = \Delta U\, t/(2h)$. All simulations were conducted on a 48×16 grid with a minimum of 32 adaptively distributed interfacial nodes.

At the initial instant, the amplitude of the interfacial wave is zero, $a = 0$. Subsequently, Marangoni stresses cause the interface to deviate from the flat position and develop a growing sinusoidal wave. Once the interfacial amplitude has grown to a significant level over an initial start-up period of time, the growth slows down, though the amplitude of the interfacial wave continues to increase while exhibiting small-amplitude oscillations despite the restoring action of surface tension. The numerical results for $\mathrm{Re} = 1$, represented by the solid line, are in good agreement with those for $\mathrm{Re} = 0$, represented by the dotted line; the latter were obtained using the boundary-element method for Stokes flow [5]. The results suggest that raising the Reynolds number slows down the initial growth of the interfacial wave due to the fluid inertia, but has only a mild effect on the growth rate at longer times. We note, in particular, that the growth curve for $\mathrm{Re} = 50$ exhibits a net decline at long times. In fact, a normal-mode stability analysis [6] reveals that, for the set of conditions presently considered, as the Reynolds number is raised from the value of unity, the growth rate of the unstable Marangoni mode increases monotonically, and rises approximately by a factor of 2·5 at $\mathrm{Re} = 50$. The superficial contrast between the numerical and analytical predictions emphasizes the difficulty of assessing flow instability from simulations beginning with an arbitrary initial state.

By way of confirming the destabilizing action of the surfactant and illustrating the nonlinear stages of the instability, we consider an initial condition in which the two layers are quiescent, and the Couette flow is established gradually by the impulsive translation of the two walls. At the initial instant, the interfacial shape is described by (4.1) with $\epsilon = 0{\cdot}2$, while the distribution of the surfactant concentration is described by (4.2) with $\epsilon_\Gamma = 0{\cdot}2$, and phase shift $\phi_\Gamma = 3\pi/2$. Figure 7 illustrates the evolution of the amplitude of the interfacial wave for layer thickness ratio $r = 2$, viscosity ratio $\lambda = 1{\cdot}0$, capillary number $\mathrm{Ca} = 2$, and negligible surfactant diffusivity, $D_s = 0$. Results are presented for Reynolds numbers $\mathrm{Re} = 1$ and 50, and surfactant sensitivity parameter $\beta = 0$ and 0·5.

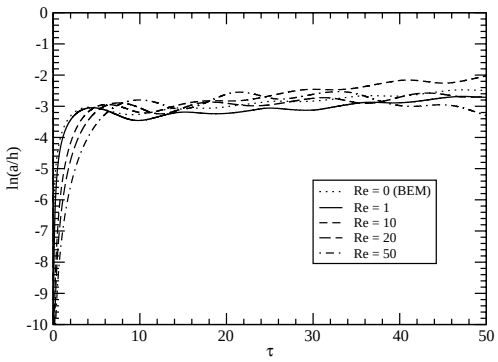

Figure 6. Effect of fluid inertia on the Marangoni instability of the two-layer Couette flow for $L/h = 6$, viscosity ratio $\lambda = 0{\cdot}5$, $\mathrm{Ca} = 2$, and negligible surfactant diffusivity.

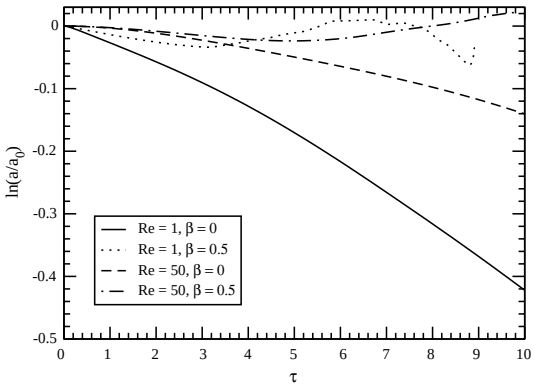

Figure 7. Destabilizing effect of a surfactant on the two-layer Couette flow for $L/h = 6$, viscosity ratio $\lambda = 1{\cdot}0$, $\mathrm{Ca} = 2$, and negligible surfactant diffusivity.

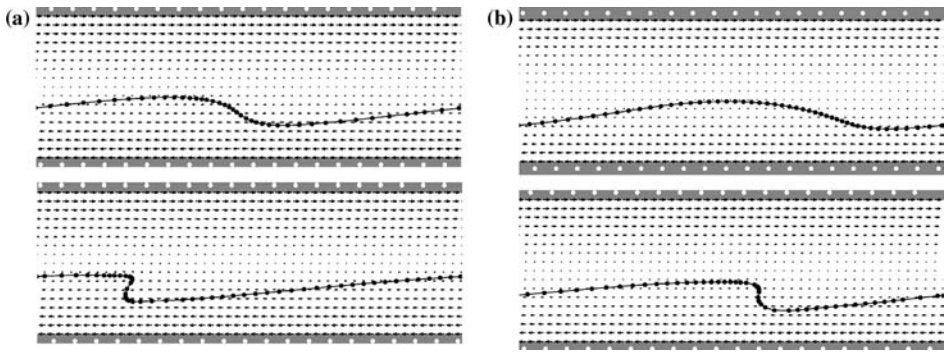

Figure 8. Stages in the Marangoni instability for $\beta = 0{\cdot}5$ and (a) $\mathrm{Re} = 1$ at time $\tau = 5{\cdot}025$ (up) and $8{\cdot}755$ (down), and (b) Re50 at time $\tau = 5{\cdot}165$ (up) and $9{\cdot}495$ (down).

When a surfactant is absent, $\beta = 0$, the interface amplitude decays monotonically under the action of surface tension for both Reynolds numbers. This behavior is consistent with the predictions of a normal-mode linear stability analysis, predicting negative growth rates at both Reynolds numbers [6]. In the presence of surfactant, the amplitude initially decays, and then it starts growing as soon as the shear flow has penetrated the layers and reached the interface. This behavior is also consistent with linear stability analysis, predicting positive growth rates for the Marangoni mode at both Reynolds numbers [6]. Figure 8 shows two stages of the motion for $\beta = 0{\cdot}5$, illustrating wave steepening and the onset of an overturning wave. The simulations were halted when a numerical instability arose due to the high interfacial curvature at the crest and base of the steep wave.

6. Discussion

The Yih instability arises at small but non-infinitesimal Reynolds numbers when the shear rate jumps across the interface due to differences in viscosity. On the other hand, the Marangoni instability arises even under conditions of Stokes flow for non-zero, but not necessarily

discontinuous, interfacial shear rates. The two modes may act synergistically or counteractively in a way that is hard to identify from circumstantial evidence extracted by solving initial-value problems.

In this article, we have investigated the effect of inertia on the Marangoni instability by numerical simulation based on the immersed interface method, and found that the Reynolds number has a mild effect on the growth of interfacial waves. To fully describe the nature of the instability, a formal linear stability analysis is required. Halpern and Frenkel [4] formulated the normal-mode linear stability problem, and displayed the Orr–Sommerfeld equations governing the growth of perturbations in the two layers and accompanying boundary and interfacial conditions. In the second part of the present study [6], numerical solutions of the eigenvalue problem will be presented, and the stability of the flow will be rigorously assessed. In particular, the predictions of the linear analysis will be found to be in excellent agreement with results of numerical simulations conducted by the immersed-interface method for a two-mode perturbation tailored to correspond to an initially flat interface.

Acknowledgements

Support for this research was provided by the National Science Foundation.

References

1. C. Pozrikidis, Instability of multi-layer channel and film flows. *Adv. Appl. Mech.* 40 (2004) In press.
2. C.S. Yih, Instability due to viscosity stratification. *J. Fluid Mech.* 27 (1967) 337–352.
3. A.L. Frenkel and D. Halpern, Stokes-flow instability due to interfacial surfactant. *Phys. Fluids* 14 (2002) 45–48.
4. D. Halpern and A.L. Frenkel, Destabilization of a creeping flow by interfacial surfactant: linear theory extended to all wavenumbers. *J. Fluid Mech.* 485 (2003) 191–220.
5. M. Blyth and C. Pozrikidis, Effect of surfactants on the stability of two-layer channel flow. *J. Fluid Mech.* 505 (2004) 59–86.
6. M.G. Blyth and C. Pozrikidis, Effect of inertia on the Marangoni instability of two-layer channel flow, Part II: normal-mode analysis. *J. Engng. Math.* 50 (2004) 329–341.
7. C. Pozrikidis, Instability of two-layer creeping flow in a channel with parallel-sided walls. *J. Fluid Mech.* 351 (1997) 139–165.
8. C. Pozrikidis, Gravity-driven creeping flow of two adjacent layers or superimposed films through a channel and down a plane wall. *J. Fluid Mech.* 371 (1998) 345–376.
9. A.V. Coward, Y.Y. Renardy, M. Renardy and J.R. Richards, Temporal evolution of periodic disturbances in two-layer Couette flow. *J. Comp. Phys.* 132 (1997) 346–361.
10. J. Li, Y.Y. Renardy and M. Renardy, A numerical study of periodic disturbances in two-layer Couette flow. *Phys. Fluids* 10 (1998) 3056–3071.
11. R.R. Yiu and K.P. Chen, Numerical experiments on disturbed two-layer flows in a channel. In: Y. Renardy, A.V. Coward, D. Papageorgiou and S.M. Sun (eds.), *Advances in Multi-Fluid Flows.* Philadelphia: SIAM (1996) pp. 368–382.
12. S. Zaleski, J. Li, R. Scardovelli and G. Zanetti, Direct simulation of multiphase flows with density variations. In: L. Fulachier, J.L. Lumley, and F. Anselmet (eds.), *IUTAM Symposium on Variable Density Low Speed Turbulent Flows.* Proc. IUTAM Symposium, Marseille, France, 1996. Dordrecht: Kluwer (1997).
13. P. Yecko and S. Zaleski, Two-phase shear instability: waves, fingers, and drops. *Ann. NY Acad. Sci.* 898 (2000) 127–143.
14. G. Tryggvason and S.O. Unverdi, The shear breakup of an immiscible fluid interface. In: W. Shyy and R. Narayanan (eds.), *Fluid Dynamics at Interfaces.* New York: Cambridge University Press (1999) pp. 142–155.
15. J. Zhang, M.J. Miksis, S.G. Bankoff and G. Tryggvason, Non-linear dynamics of an interface in an inclined channel. *Phys. Fluids* 14 (2002) 1877–1885.
16. C.S. Peskin, The immersed boundary method. *Acta Numer*. 11 (2002) 479–517.

17. K. Sheth, and C. Pozrikidis, Effects of inertia on the deformation of liquid drops in simple shear flow. *Comput. Fluids* 24 (1995) 101–119.
18. C. Pozrikidis, *Introduction to Theoretical and Computational Fluid Dynamics.* New York: Oxford University Press (1997) 675 pp.
19. X. Li and C. Pozrikidis, The effect of surfactants on drop deformation and on the rheology of dilute emulsions in Stokes flow. *J. Fluid Mech.* 341 (1997) 165–194.
20. S. Yon and C. Pozrikidis, A finite-volume/boundary-element method for flow past interfaces in the presence of surfactants, with application to shear flow past a viscous drop. *Comput. Fluids* 27 (1998) 879–902.
21. A.W. Adamson, *Physical Chemistry of Surfaces.* 5th edn., New York: Wiley (1990) 777 pp.
22. C. Pozrikidis, *Numerical Computation in Science and Engineering.* New York: Oxford Univ. Press (1998) 627 pp.
23. C. Pozrikidis, On the relationship between the pressure and the projection function for the numerical computation of incompressible flow. *Euro. J. Mech. B/Fluids* 22 (2003) 105–121.
24. C.S. Peskin, Numerical analysis of blood flow in the heart. *J. Comp. Phys.* 25 (1977) 220–252.